A multi-atlas based method for automated anatomical Macaca fascicularis brain MRI segmentation and PET kinetic extraction

Benedicte Ballanger, Léon Tremblay, Véronique Sgambato-Faure, Maude Beaudoin-Gobert, Franck Lavenne, Didier Le Bars, Nicolas Costes

NeuroImage 77 (2013) 26–43

Contents lists available at SciVerse ScienceDirect

NeuroImage

journal homepage: www.elsevier.com/locate/ynimg

A multi-atlas based method for automated anatomical *Macaca fascicularis* brain MRI segmentation and PET kinetic extraction

Bénédicte Ballanger [a,b], Léon Tremblay [a,b], Véronique Sgambato-Faure [a,b], Maude Beaudoin-Gobert [a,b], Franck Lavenne [c], Didier Le Bars [b,c], Nicolas Costes [c,*]

[a] Centre National de la Recherche Scientifique, Centre de Neurosciences Cognitives, UMR 5229, Bron, France
[b] Université Claude Bernard-Lyon 1, Université de Lyon, 69622, Lyon, France
[c] CERMEP - Imagerie du vivant, Lyon, France

ARTICLE INFO

Article history:
Accepted 13 March 2013
Available online 26 March 2013

Keywords:
Macaca fascicularis
Atlas
Template
Brain
PET
MRI

ABSTRACT

MRI templates and digital atlases are needed for automated and reproducible quantitative analysis of non-human primate PET studies. Segmenting brain images *via* multiple atlases outperforms single-atlas labelling in humans. We present a set of atlases manually delineated on brain MRI scans of the monkey *Macaca fascicularis*. We use this multi-atlas dataset to evaluate two automated methods in terms of accuracy, robustness and reliability in segmenting brain structures on MRI and extracting regional PET measures.

Methods: Twelve individual *Macaca fascicularis* high-resolution 3DT1 MR images were acquired. Four individual atlases were created by manually drawing 42 anatomical structures, including cortical and sub-cortical structures, white matter regions, and ventricles. To create the MRI template, we first chose one MRI to define a reference space, and then performed a two-step iterative procedure: affine registration of individual MRIs to the reference MRI, followed by averaging of the twelve resampled MRIs. Automated segmentation in native space was obtained in two ways: 1) Maximum probability atlases were created by decision fusion of two to four individual atlases in the reference space, and transformation back into the individual native space (MAXPROB). 2) One to four individual atlases were registered directly to the individual native space, and combined by decision fusion (PROPAG). Accuracy was evaluated by computing the Dice similarity index and the volume difference. The robustness and reproducibility of PET regional measurements obtained via automated segmentation was evaluated on four co-registered MRI/PET datasets, which included test–retest data.

Results: Dice indices were always over 0.7 and reached maximal values of 0.9 for PROPAG with all four individual atlases. There was no significant mean volume bias. The standard deviation of the bias decreased significantly when increasing the number of individual atlases. MAXPROB performed better when increasing the number of atlases used. When all four atlases were used for the MAXPROB creation, the accuracy of morphometric segmentation approached that of the PROPAG method. PET measures extracted either via automatic methods or via the manually defined regions were strongly correlated, with no significant regional differences between methods. Intra-class correlation coefficients for test–retest data were over 0.87.

Conclusions: Compared to single atlas extractions, multi-atlas methods improve the accuracy of region definition. They also perform comparably to manually defined regions for PET quantification. Multiple atlases of *Macaca fascicularis* brains are now available and allow reproducible and simplified analyses.

Introduction

Functional neuroimaging studies on non-human primates have become key tools for studying the pathogenesis and progression of neurological diseases (Blesa et al., 2012; Neumane et al., 2012). Until recently, these studies were analysed mainly as case reports (Black et al., 1997). This approach, while valid, does not take advantage of the powerful multi-subject methods of averaging brains in a common atlas space. In the same vein, manual labelling of regions of interest (ROI) (Brown et al., 2012; Nagai et al., 2012), although widely used up to now in those studies, is expert-dependent, demanding for observers, and time consuming. Essentially, manual labelling is not transferable and thus is not suitable for large datasets. Accordingly, an important step forward is to extend single-subject reports to multi-subject investigations. These can address the inter-subject variability and generalizability of findings as they are widely performed in human positron emission tomography (PET) studies (Fox et al., 1985; Friston et al., 1995). Implementing automated methods of delineation that minimise operator dependence is highly desirable. A strategy of template use with a digital multi-atlas approach for effective automated unseen brain ROI segmentation has been

* Corresponding author at: CERMEP, 59 boulevard Pinel, 69677 Bron Cedex, France. Fax: +33 472 68 86 10.
E-mail address: costes@cermep.fr (N. Costes).

1053-8119/$ – see front matter © 2013 Elsevier Inc. All rights reserved.
http://dx.doi.org/10.1016/j.neuroimage.2013.03.029

proposed for the human brain (Hammers et al., 2002, 2003). By computing a maximum probability atlas in a common space by fusion of multiple individual atlases, the multi-atlas method outperforms single-atlas approaches. Moreover the multi-atlas method has been significantly improved by the propagation–fusion of the multi-atlas dataset in the individual space of the brain to be segmented (Heckemann et al., 2006). These multi-atlas strategies may be applicable to the non-human primate brain. They require a common space, with a normalisation template, and a multi-atlas dataset, and sufficient individuals. Magnetic resonance imaging (MRI) templates are currently available for such species as baboons (Black et al., 2001b; Greer et al., 2002), pig-tailed macaques (*Macaca nemestrina*) (Black et al., 2001a), rhesus monkeys (*Macaca mulatta*) (McLaren et al., 2009), chimpanzees (Rilling et al., 2007), Japanese macaques (*Macaca fuscata*) (Quallo et al., 2010), and more recently, marmoset monkeys (Hikishima et al., 2011), and cynomolgus monkeys (*Macaca fascicularis*) (Collantes et al., 2009; Frey et al., 2011). It has been recognised that there are differences, although subtle, between the brain structures of different macaque species (Van Der Gucht et al., 2006). For instance, differences in skull shape are noticeable between the cynomolgus and the rhesus monkeys (Frey et al., 2011; McLaren et al., 2009). These affect the temporal and frontal lobes, which could be of importance in the results of some studies using techniques such as voxel-based-morphometry. To date, no multi-atlas dataset has been available for non-human primates. We chose the *Macaca fascicularis* model since this monkey represents the most relevant animal model of human brain pathology (Worbe et al., 2013), such as the parkinsonian syndromes induced by MPTP lesion (Neumane et al., 2012).

In this paper we introduce a set of manually created *Macaca fascicularis* brain atlases. With this multi-atlas dataset, we evaluate the accuracy, robustness and reliability of two automated methods for segmenting brain structures and extracting regional PET measurements.

Material and methods

Animals

Twelve healthy cynomolgus monkeys (*M. fascicularis*) were studied (six males and six females, three to five years old, weight = 5 ± 1 kg). Four of those animals (all males, three to 4.5 years old, weight = 5 ± 1 kg) were used to create the multi-atlas dataset, and underwent dynamical functional PET acquisitions with different radiotracers.

On the day of the experiment, each animal was pre-treated with Atropine (0.05 mg/kg) and 15 minutes later anaesthetized by an intramuscular dose of Zoletil (15 mg/kg). The animal remained under this anaesthesia for the MRI scan. For the PET scan, a lactated Ringer's solution was continuously infused through a saphenous vein catheter. Monkeys were then transported to the Imaging Centre (CERMEP, Lyon, France) where they were placed in MRI- and PET-compatible stereotaxic apparatus. The care and treatment of the monkeys were in strict accordance with NIH guidelines (2011) as well as with the European Community Council Directive of 1986 (86/609/EEC) and the recommendations of the French National Committee (87/848).

MRI Protocol

For each animal, three high-resolution (0.6 x 0.6 x 0.6 mm^3) 3D T1-weighted MRI scans were acquired with a 1.5 T Sonata Siemens scanner, and averaged for noise reduction contrast enhancement. T1 weighted axial images were acquired using a MPRAGE sequence with the following acquisition parameters: TE = 2.89 ms, TR = 2160 ms, IT = 1100 ms, flip angle = 15°, 176 sagittal slices, FoV = 154 mm, matrix size = 256x256, slice thickness = 0.6 mm, time of acquisition = 13.51 x 3.

PET Protocol

PET scans were performed in three-dimensional (3D) mode using a Siemens CTI HR + tomograph, with an axial field of view of 15.2 cm, yielding 63 planes and a nominal in-plane resolution of 4.1 mm full-width-at-half-maximum (FWHM) according to the NEMA protocol (Brix et al., 1997). Before the tracer injection, a transmission scan (^{68}Ge rotating rod sources; 10 min) was acquired to correct for tissular 511 keV gamma attenuation. The tracers used were [^{11}C]Raclopride for studying dopamine D2 receptor binding, 2′-methoxyphenyl-(*N*-2′-pyridinyl)-*p*-^{18}F-fluoro-benzamidoethylpiperazine ([^{18}F]MPPF) for 5-HT_{1A} receptor binding, and [11C]*N*,*N*-dimethyl-2-(2-amino-4-cyanophenylthio)benzylamine (DASB) for serotonin transporter binding. Dynamic acquisition started with the i.v. injection of the radiotracer (133.2 ± 24.8 MBq for [^{11}C]Raclopride, 154.3 ± 16.3 MBq for [^{11}C]DASB, and 107.3 ± 16.6 MBq for [^{18} F]MPPF). Respiratory frequency, pO2 and heart rate were monitored throughout the experiment. The 3D emission data were reconstructed with attenuation and scatter correction by a 3D filtered back projection (Hamming filter; cut-off frequency, 0.5 cycles/pixel) algorithm and a zoom factor of three. Reconstructed volumes were 128 × 128 matrices of 0.32x0.32 mm^2 pixels in sixty-three 2.42 mm spaced planes.

MRI Template creation

An MRI template was constructed from the images of six males and six females *M. fascicularis* monkeys (Fig. 1). One of the individual MRI scans (Reference MRI, average of four 3D T1-MRI acquisitions of the same animal) was selected as the representative brain, and manually oriented in the anterior–posterior commissure (AC-PC) transverse plane. The space of this reference MRI would further constitute the reference space. All MRI were skull-stripped using the brain extraction with bet (FSL; Smith, 2002). 3D affine co-registration on the reference MRI was performed in two steps: a manual reorientation to the reference scan using identified homologous landmarks, including: the centre of the left and right eyeballs, the anterior commissure (AC), the posterior commissure (PC), the posterior apex of the 4th ventricle as seen in a midline sagittal image, and the intersection of the central sulcus with the longitudinal fissure. This manual registration was followed by an automated registration with mutual information as a similarity index, and simplex optimization (*minctracc*, Collins et al., 1994). Tri-linear resliced co-registered MRIs were then averaged (*mincaverage*) with normalise intensity.

Individual atlases creation

Individual atlases were created from the MRIs of four animals by manually labelling 42 brain structures in three dimensions, following a precise delineation protocol (Table 1 and Appendix A). All delineations were performed in native space, i.e., before spatial transformation into reference space. Each ROI was manually drawn on the individual MRI by two operators (BB, MBG) with the help of *M. fascicularis* brain atlases (Lanciego and Vázquez, 2011; Martin and Bowden, 1996; Szabo and Cowan, 1984).

Maximum probability atlases creation

Individual atlases were transformed in the reference space by applying spatial transformation of individual MRIs from native space to reference space. We interpolated into 0.6 mm square voxels by using the nearest neighbour interpolation to preserve label values (Fig. 2A). A maximum probability (MAXPROB) atlas was computed form the resampled atlases in the reference space, obtained by the fusion with a maximum frequency rule at a voxel level as performed by Hammers et al. (2003). Eleven MAXPROB atlases were created based on two (six

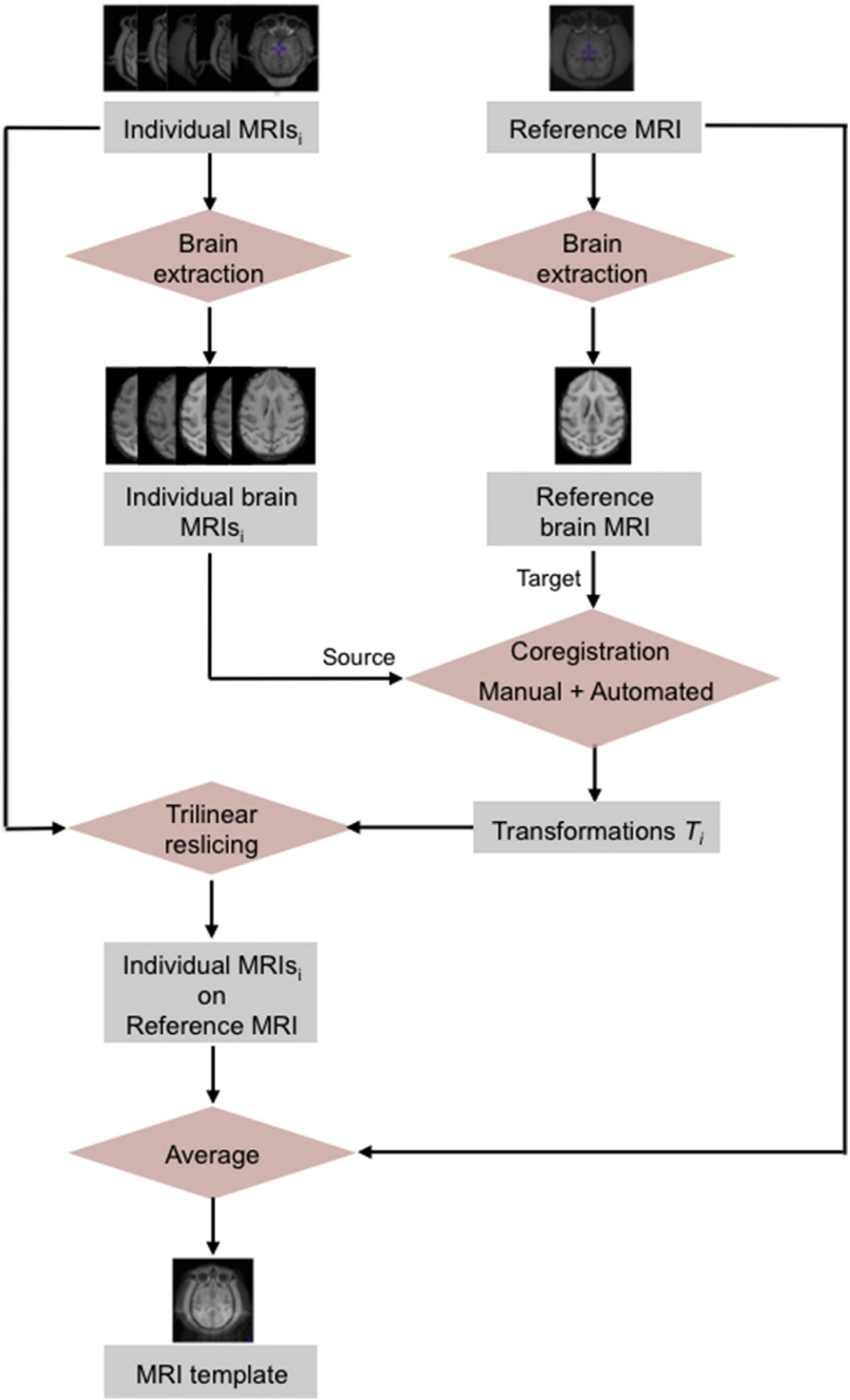

Fig. 1. Synopsis of the MRI template creation in four steps: brain extraction, coregistration of the individual brain MRIs on a reference MRI, tri-linear interpolation of the coregistered individual brains, and averaging in the reference space to form the MRI template.

Table 1
List of labelled brain structures (n = 42, second column), pooled by region group (first column) with the corresponding areas (last column, see Saleem and Logothetis, 2007). L = left side, R = right side.

Region groups	Anatomical regions	Label numbers	Corresponding areas
1 — Basal Ganglia	Anterior Caudate Nucleus (R + L)	1, 2	
	Anterior Putamen (R + L)	3, 4	
	Ventral Striatum (R + L)	5, 6	
	External Pallidum (R + L)	7, 8	
	Internal Pallidum (R + L)	9, 10	
	Posterior Caudate Nucleus (R + L)	11, 12	
	Posterior Putamen (R + L)	13, 14	
	Ventral Posterior Putamen (R + L)	15, 16	
	Substantia Nigra (R + L)	17, 18	
	Thalamus (R + L)	19, 20	
2 — Cingulate Cortex	Anterior Cingulate Cortex (R + L)	33, 34	24, 32
	Limbic Cingulate Cortex (R + L)	35, 36	25
	Posterior Cingulate Cortex (R + L)	37, 38	23, 29, 30, 31
3 — Frontal Cortex	Dorsolateral Frontal Cortex (R + L)	39, 40	9d, 46d
	Medial Frontal Cortex (R + L)	69, 70	9 m, 10 m, 14c, 14r
	Orbitofrontal Cortex (R + L)	31, 32	10o, 11 m, 12o, 13, 14
	Ventral Frontal Cortex (R + L)	63, 64	12 l, 44, 45, 46v, 8a (FEF)
4 — Occipital Cortex	Occipital Cortex (R + L)	49, 50	V1, V2, V3, V4
5 — Parietal Cortex	Inferior Parietal Cortex (R + L)	53, 54	
	Precuneus (R + L)	55, 56	7 m
	Superior Parietal Cortex (R + L)	51, 52	7a/b
6 — Sensorimotor Cortex	Premotor Cortex (R + L)	57, 58	F2, F3, F4, F5, F6. F7
	Primary Motor Cortex (R + L)	59, 60	4 (F1)
	Primary sensory Cortex (R + L)	61, 62	1, 2, 3a/b, 5
7 — Temporal Cortex	Enthorinal Cortex (R + L)	67, 68	28
	Fusiform Gyrus (R + L)	65, 66	
	Parahippocampal Gyrus (R + L)	41, 42	
	Inferior Temporal Cortex (R + L)	47, 48	
	Medial Temporal Cortex (R + L)	45, 46	
	Superior Temporal Cortex (R + L)	43, 44	
8 — Limbic Structures	Amygdala (R + L)	23, 24	
	Insula (R + L)	27, 28	
	Hippocampus (R + L)	21, 22	
9 — Brain Stem	Brain Stem	84	
10 — Cerebellum	Cerebellum (R + L)	29, 30	
	Vermis	72	
11 — Cerebellum White Matter	Cerebellum White Matter	88	
12 — White Matter	White Matter Top Part (R + L)	80, 81	
	White Matter Bottom Part (R + L)	82, 83	
13 — Ventricles	Lateral Ventricles (R + L)	85, 86	
	Third & Fourth Ventricles	87	
14 — Cerebrospinal Fluid	Cerebrospinal Fluid	89	

combinations), three (four combinations) or the four (one combination) individual atlases.

Propagated atlas creation

A propagated atlas is the fusion of individual atlases, propagated by spatial normalisation from their native space to the native space of an individual. Accordingly, we were able to create a propagated atlas for each of four individuals (Fig. 2B), made by the fusion of the four individual atlases.

Automated segmentation methods

MAXPROB method

Automated segmentation of an individual MRI with a maximum probability atlas is achieved by (1) Computing the spatial normalisation of its MRI on the MRI template in the reference space with *minctracc*, (2) Computing the inverse transform matrix from the reference space to the individual space, and (3) Reslicing the maximum probability atlas in the native space, by applying the inverse transform with nearest neighbour interpolation to preserve label values. The MAXPROB method has been tested with the combination of one (MAXPROB_1), two (MAXPROB_2), three (MAXPROB_3) and four (MAXPROB_4) individual atlases.

PROPAG method

Automated segmentation with a propagated atlas is simply the extraction of region with the propagated atlas, which is by definition in the individual space. The PROPAG method has been tested with a propagated atlas composed of four individual atlases (PROPAG_4).

Atlas evaluation

We evaluated the methodology of using automated atlases for MRI regional brain structure segmentation and for value extraction from a PET image. To do so we used two approaches:

Morphometric evaluation

Accuracy of morphometric segmentation was evaluated by comparing the manual delineation of selected brain structures (basal ganglia, brain stem, CSF, cerebellum, cerebellum_white matter, frontal cortex, limbic system, cingulate cortex, motor cortex, occipital cortex, parietal cortex, temporal lobe, and ventricles) with the delineation obtained using automated segmentation.

Two morphometric indices were used. The *Dice index*, as an index of the overlap of automated brain structure extraction and the manual structure extraction (Similarity Index (SI); Eq. (1)), and the relative *volume difference* (Δvol; Eq. (2)) as the bias in

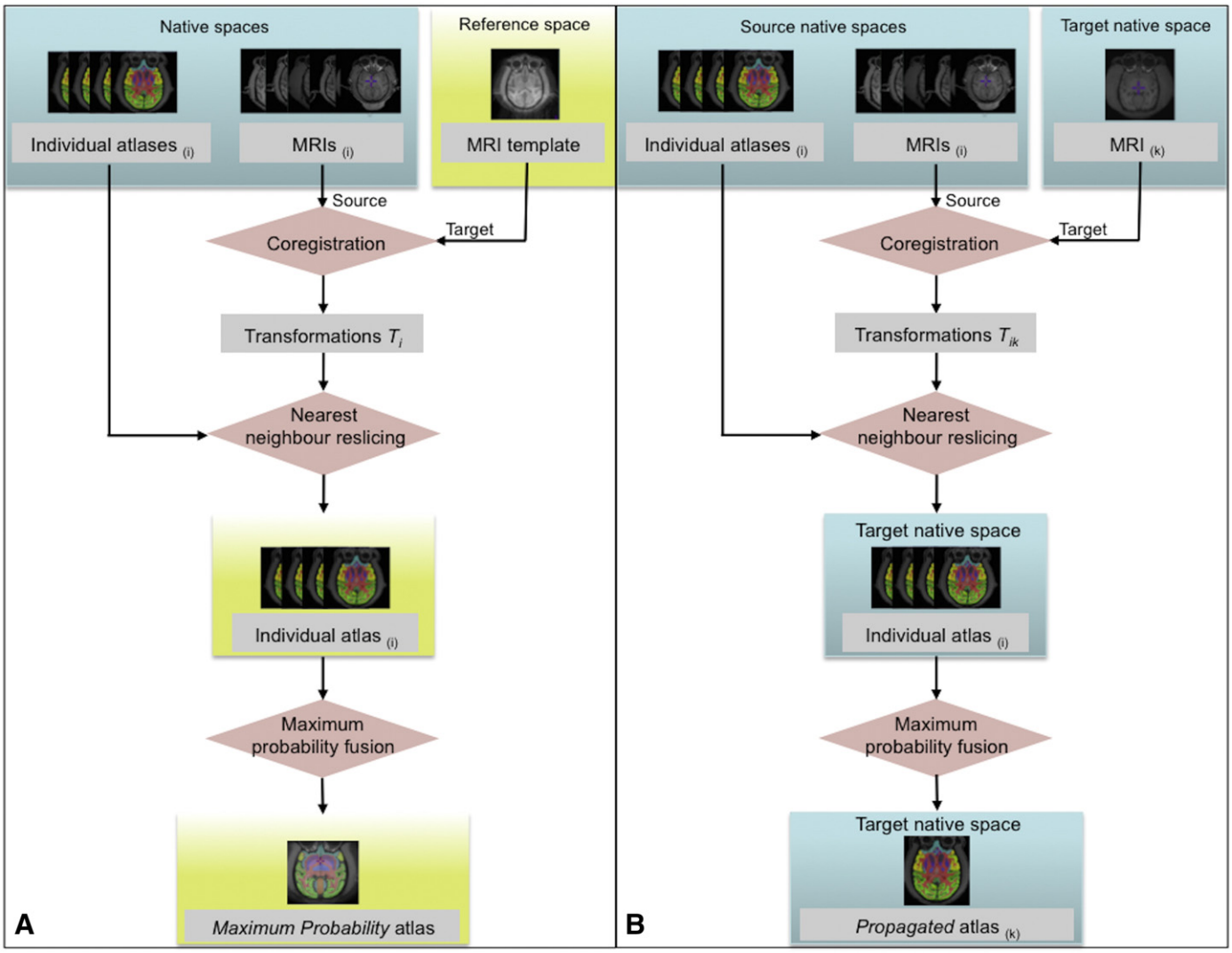

Fig. 2. Synopsis of the maximum probability (MAXPROB) atlases (A), and the propagated atlases (B) creation. In (A), individual MRIs are coregistered to the template MRI. Transformations are used to reslice the individual atlases with nearest neighbour interpolation method. Then coregistered atlases are fused with a maximum probability rule to form the MAXPROB atlas. In (B), individual MRIs are directly coregistered to the target MRI. The individual atlas fusion is then performed in the native space of the target MRI to form the propagated atlas.

volume of the brain structures extracted by manual and by automated delineation.

$$SI = 2x\left(\frac{Nautomated \cap manual}{Nautomated + Nmanual}\right) \quad (1)$$

$$\Delta vol = \left(2x\frac{Nautomated - Nmanual}{Nautomated + Nmanual}\right)x100 \quad (2)$$

Morphometric evaluation was tested with the eleven possibilities of segmenting an individual with the MAXPROB method (leaving out the maximum probability atlas containing the individual itself; except for the MAXPROB_4, which necessarily contained the four individual atlases) and one possibility of segmenting with the PROPAG method.

Functional evaluation

To allow comparison between manual and automatic extraction, the accuracy of regional brain PET binding quantification with various tracers was evaluated on the four animals for which we had made the individual atlases. Those animals were scanned before and after MPTP intoxication (Table 2). Individual PET data were registered to individual MRI data by computing the rigid spatial transformation between the PET summed image and the MRI. PET kinetic extraction was achieved using (1) the manually drawn ROIs, (2) the automated ROIs generated by segmentation with the MAXPROB_4 method, and (3) the automated ROIs generated by segmentation with the PROPAG_4 method. The simplified tissue reference tissue model (SRTM, Gunn et al., 1997) was used for tracer quantification, using the cerebellum as reference region. The accuracy of quantification was evaluated on the regional non-displaceable binding potential (BP_{ND}). Bias (Eq. (3), that is an index of the quantification bias between manual method and automated method) and intra-class coefficients (ICC) of the BP_{ND} were computed, as well as the standard deviation (SD) of the bias which reflected the variability of the reproducibility between methods. The ICC, in the present study, was an index of the reproducibility of values by comparing between method variability to within method variability, and was computed with the classical formulae (BSMSS – WSMSS)/(BSMSS + WSMSS), where BSMSS is the between method mean sum of square and WSMSS the within method mean sum of square. Tested regions were a selection of representative brain structures for each tracer.

$$Bias = 100x\frac{BPmanual - BPautomated}{BPmanual} \quad (3)$$

Table 2
Number of PET scans used in the functional evaluation for each of the four monkeys (MF) scanned when in a MPTP protocol.

	Before MPTP Intoxication				After MPTP Intoxication			
	MF1	MF2	MF3	MF4	MF1	MF2	MF3	MF4
[^{11}C]DASB			2		2		4	3
[^{18} F]MPPF		2	1	1		2	2	2
[^{11}C]Raclo	2	1	1	1	2	2	2	2

Statistical analysis

All statistical analyses were performed using STATA 8 (StataCorpLP, College Station, TX, USA). The significance threshold was set at $P < 0.05$ with Scheffe adjustment in post-hoc comparisons.

Results

Using the methodology described above, we created a brain *Macaca fascicularis* template and its reference atlas (Fig. 3, column 1 and 2), i.e. the maximum probability (MAXPROB) atlas obtained from the fusion of four individuals. These data are available for research use from http://www.cermep.fr/download/atlas. This standard *M. fascicularis* MRI template that we obtained allows spatial normalisation to a common space of individual MRI studies, providing an excellent spatial fit between images with automatic procedures.

Morphometric evaluation

Are regional volumes extracted by automated delineation dependent on the number of atlases used in the segmentation method?

The one-way ANOVA on regional volumes with number of atlases as the fixed effect, by region group, showed no difference whatever between the number of atlases except for the brainstem ($F(4,35) = 2,73$, $p = 0.048$) but without significant post-hoc comparisons.

Is there a morphometric difference between segmented volumes with manual delineation compared to automated delineation?

The boxplots of volume difference (%), split by region group and by number of atlases constituting the maximum probability atlases (MAXPROB_1 to MAXPROB_4) and the PROPAG_4 atlases are shown in Fig. 4. No systematic bias in volume measurement between manual and automated methods was observed except for an overestimation in the limbic system (+4.8%, $t(1,23) = 2.17$, $p < 0.04$ for the MAXPROB_4 method and +4.9%, $t(1,23) = 2.26$, $p < 0.03$ for the PROPAG_4 method) and the occipital cortex (+4.9%, $t(1,7) = 2.54$, $p < 0.04$, for the PROPAG_4 method).

The analysis of the standard deviation (SD) of the volume difference showed (Fig. 5) that increasing the number of individual atlas reduced its variability. We performed variance ratio tests that compared the variance of the volume difference in the MAXPROB_1 *versus* PROPAG_4 methods, MAXPROB_2 *versus* PROPAG_4 methods, MAXPROB_3 *versus* PROPAG_4 methods and MAXPROB_4 *versus* PROPAG_4 methods. It showed that at least two atlases with the MAXPROB method were needed to reach the SD of the PROPAG method regarding the volume segmentation of the cingulate, the limbic, the parietal, temporal, and the ventricles region groups. For the motor cortex, at least three atlases were needed, while for the basal ganglia and the frontal cortex regions four atlases were needed. In other words, the more atlases, the less dispersion in percent volume differences between automated and manual segmentation was induced.

Overlap between automated and manually delineated regions

The bar plot of the segmentation accuracy performance is shown in Fig. 6. For an automated segmentation with one atlas, the Dice index (SI) goes from 0.49 for the ventricles and the cerebellum_white matter region groups to 0.74 for the brain stem region. Using four individual atlases and the MAXPROB method, SI goes from 0.69 for the ventricles and the cerebellum white matter region groups to 0.85 for the brainstem region. Performances were around 0.8 for the basal ganglia, the limbic system, the cerebellum and the white matter region groups as well as the frontal, motor and occipital cortices. By increasing the number of individual atlases from one to four we achieved substantially higher SIs (Table 3). This clearly showed that maximum performances were reached with more than three atlases. With the PROPAG method and four individual atlases, results were slightly but not significantly better, except for the frontal cortex (0.79 with PROPAG *versus* 0.80 with the MAXPROB method).

The performance for each ROI is presented in Fig. 7. It shows that within the basal ganglia region group, the small regions such as the substantia nigra, the ventral posterior putamen, the ventral striatum, and the internal pallidum are 15–20% inferior to other ROIs of this group. Performances in the limbic structures, the frontal, the motor, the parietal, and the temporal groups are quite homogenous. Some heterogeneity in region groups reduced the performances, such as the limbic anterior cingulate cortex in the cingulate cortex, and the fusiform, the parahippocampic, and the enthorinal cortices in the temporal lobe. There was no correlation between the Dice indices and the region volumes ($R^2 = 0.00029$).

Functional evaluation

The automated methods were evaluated by comparing BP_{ND} determined using: (1) manually drawn ROIs of the individual, (2) automated ROIs generated with the MAXPROB_4 method, and (3) automated ROIs generated with the PROPAG_4 method.

Regression analysis of BP_{ND} for the [^{11}C]DASB, the [^{18} F]MPPF, and the [^{11}C]Raclopride studies are shown in Fig. 8. The first raw shows quite a good correlation ($R^2 = 0.67$) for the DASB quantification and a small underestimation (5%) with the MAXPROB_4, and a good correlation ($R^2 = 0.89$) and a small overestimation (+5%) with the PROPAG_4 method. For the [^{18} F]MPPF, correlation is excellent with the MAXPROB_4 ($R^2 = 0.95$) and the PROPAG_4 method ($R^2 = 0.97$), as well as for [^{11}C]Raclopride and the MAXPROB_4 ($R^2 = 0.95$) or the PROPAG_4 ($R^2 = 0.95$) methods. In addition, the estimation errors were less than one percent on average whatever the method and the tracer used. In Table 4, regional bias, standard deviations and ICC are given for the control scans of the [^{18} F]MPPF, and the [^{11}C]Raclopride acquisitions. The number of control scans for the [^{11}C]DASB ($n = 2$) was not sufficient to compute reliable estimations. For the [^{18} F]MPPF, with the MAXPROB_4 method, the bias went from −1.5% to 5.8% and the variability did not exceed 20% (maxima 19.2% for the occipital cortex, 16.6% for the anterior cingulate cortex, and 16.5% for the amygdala). With the PROPAG_4 method, the bias went from −3% to 4.5%, the variability did not exceed ten percent, and was approximately divided by two compared to the MAXPROB_4 method ($p < 0.0001$). For the [^{11}C]Raclopride, reproducibility results with the MAXPROB_4 and the PROPAG_4 methods were quite similar ($p = 0.15$), with a mean bias of plus or minus 0.5%, and a variability around ten percent. A comparison of reproducibility performances between MAXPROB_4 and PROPAG_4 showed no significant differences for the bias ($p = 0.08$), and for the SD of the bias ($p = 0.46$). The ICC gave the reliability of using the manual or automated method for quantification. For the [^{18} F]MPPF, it was on average 0.77 for the MAXPROB_4 method, and was significantly ($p < 0.0007$) improved by twenty percent

Fig. 3. Coronal views of the MRI template (column 1), the maximum probability (MAXPROB_4) atlas composed by the four individuals (column 2), the individual atlases (column three to six). Views are taken from the individual atlases resampled in the reference space. Slices are 3 mm apart (one slice out of five).

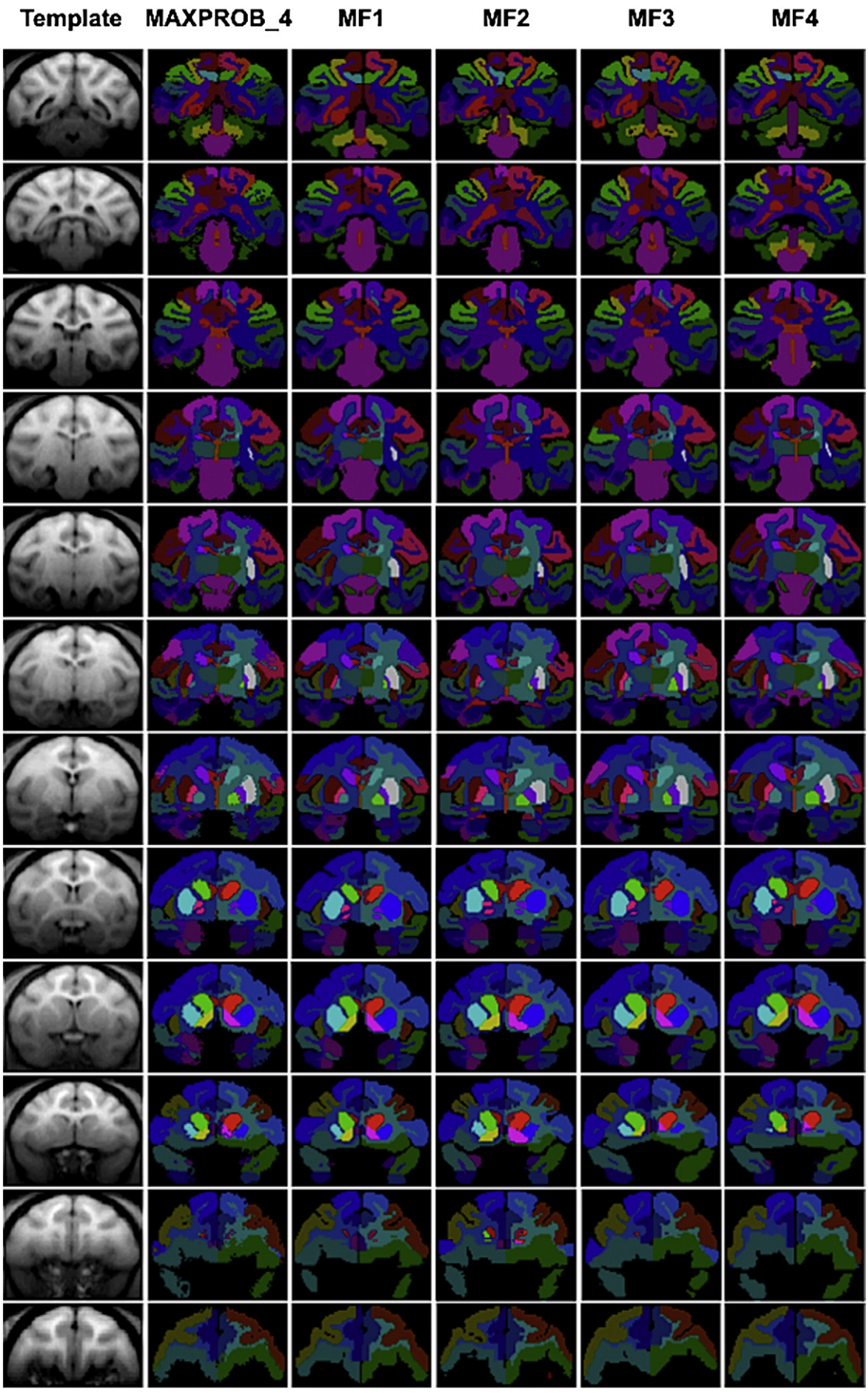
Template
MAXPROB_4
MF1
MF2
MF3
MF4

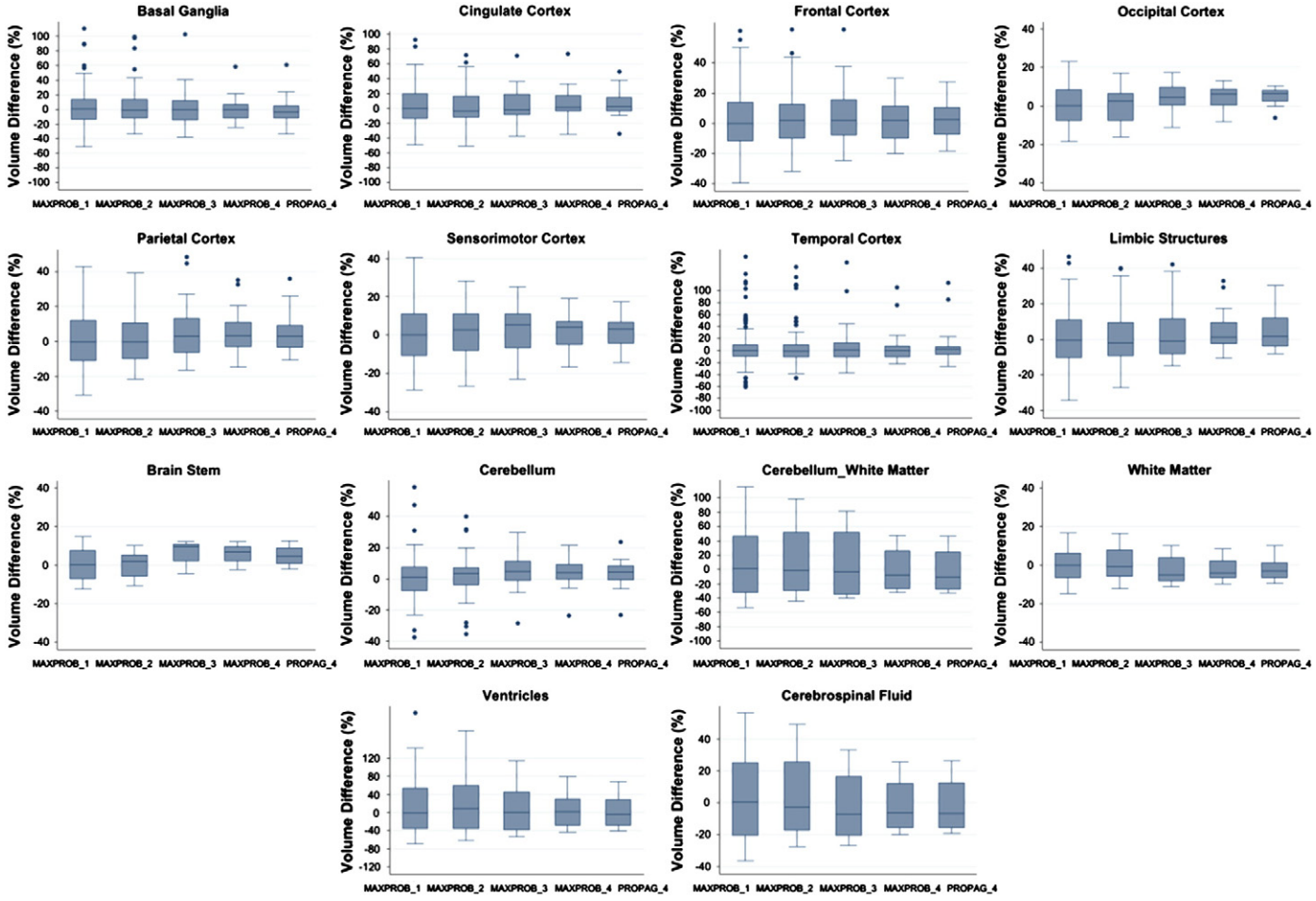

Fig. 4. Box-plots of the volume difference between the manual delineation of brain structures, and their automated segmentation. Graphs are divided by regional group of brain structures (Table 1). Two automated methods using multi-atlas dataset are tested: MAXPROB and PROPAG. Results with MAXPROB are given for a number of individual atlases from one to four. Results with PROPAG are shown for the use of four individual atlases.

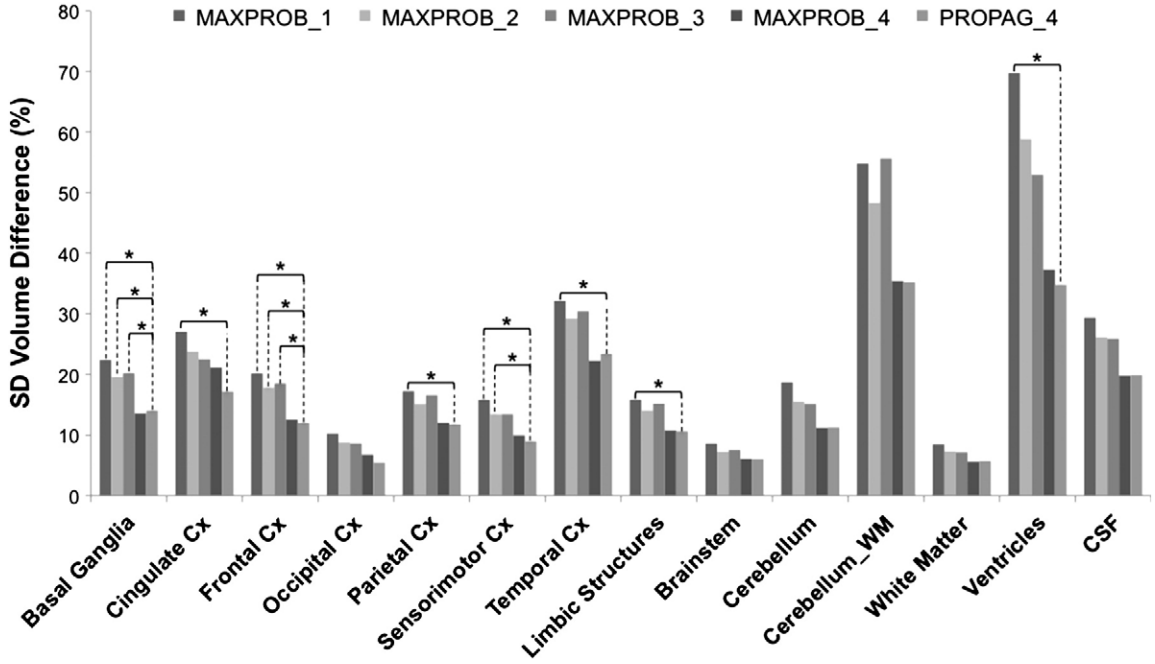

Fig. 5. Bar plot of standard deviation (SD) of the volume difference expressed in percentage (%) and represented by region group for all maximum probability atlases. Stars are showing significant difference in a variance ratio test with the SD of the PROPAG_4 method.

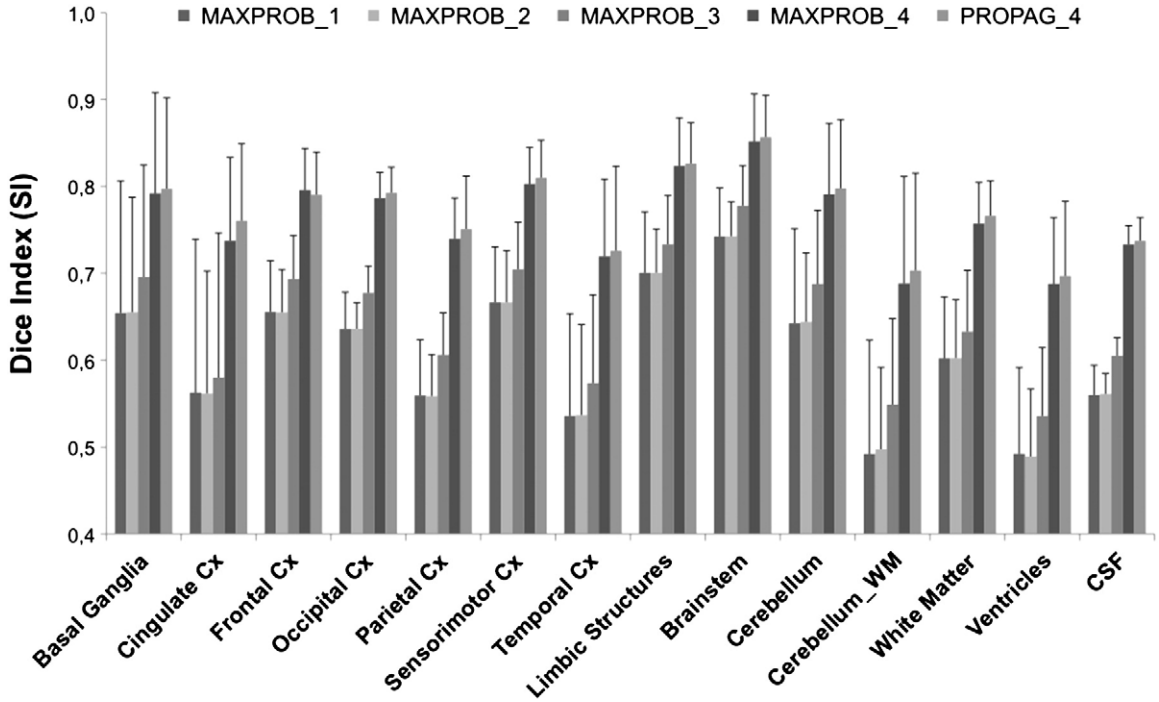

Fig. 6. Bar plot representation of the Dice index (SI) by region group and by method. Error bars are standard deviations.

with the PROPAG_4 method (average 0.92). For the [^{11}C]Raclopride, we found very high correlations between BP_{ND} values obtained from manual delineation of the ROIs and those obtained using the automated methods in all the subdivisions structures of the striatum (ICC > 0.82). There were no significant improvements when using the ICC ($p = 0.11$) of the MAXPROB_4 and the PROPAG_4 methods.

Discussion

The objective of this study was to create a set of manually delineated atlases that is needed to quantify multi-subjects PET studies in an automated and reproducible manner. Accordingly, we used MRI volumes from a group of four normal adult cynomolgus monkeys to create the individual atlases.

This study produced several notable results. First, automated segmentation did not induce bias for absolute volume measurement and regional delineations between the two automated segmentation were comparable for all region groups when tested with four individual atlases. Second, this study found that both MAXPROB and PROPAG automated segmentation were highly efficient and capable of yielding reproducible functional quantification with an accuracy comparable to manual segmentation. Third, the reliability study (ICC) showed that the choice between our two automated segmentation methods depended on the PET tracer used. For instance the reliability of the measurement with the PROPAG method was considerably increased by the reproducibility of the delineation for spreading tracers of grey matter.

Accuracy of morphometric segmentation

This study showed that automated segmented volumes of all region groups were comparable to manually segmented volumes. However, the MAXPROB_4 and PROPAG_4 methods overestimated by 5% the volumes of the limbic system. In addition, the volume of the occipital cortex was also slightly overestimated by 5% with the PROPAG_4 method. Therefore, absolute volumetric analysis of the limbic system and occipital cortex will require more caution since the automated methods introduce a positive bias of 5% compared to manual delineation. Nevertheless, this conclusion has to be taken with caution since the sensitivity of the evaluation method using four atlases is based on a small number of cases compared to the evaluation of segmentation with two or three individual atlases. Furthermore, our results demonstrated that the use of multi-atlas segmentation significantly reduces the standard deviation of the bias, thereby strengthening the reliability of volume measurement. Specifically, we showed that this improvement is efficient for sub-cortical structures (i.e. basal ganglia) as well as the frontal cortex (Table 1). Given that the *M. fascicularis* monkey represents the most relevant animal model of Parkinson's disease, we conclude that the multi-atlas automated method for volumetric studies will be essential for accurate results.

In terms of spatial delineation of regions, our results showed that the use of single subject atlas did not provide satisfactory results. This finding was also true for automated segmentation with two or three atlases. However, with more than three individual atlases, automatically and manually defined structures overlapped with a dice index

Table 3
Results of the post-hoc comparisons between methods, for the Dice index according to the number of individual atlases. (* for significant comparisons, NS = Non Significant).

Region Groups	*versus*	MAXPROB_1	MAXPROB_2	MAXPROB_3	MAXPROB_4
Basal Ganglia, Cingulate, Frontal, Sensorimotor, Occipital, Parietal, Temporal Cortices, Limbic Structures, White Matter, Ventricles, CSF	MAXPROB_4	*	*	*	
	PROPAG_4	*	*	*	NS
Brainstem, Cerebellum	MAXPROB_4	*	*	NS	
	PROPAG_4	*	*	NS	NS

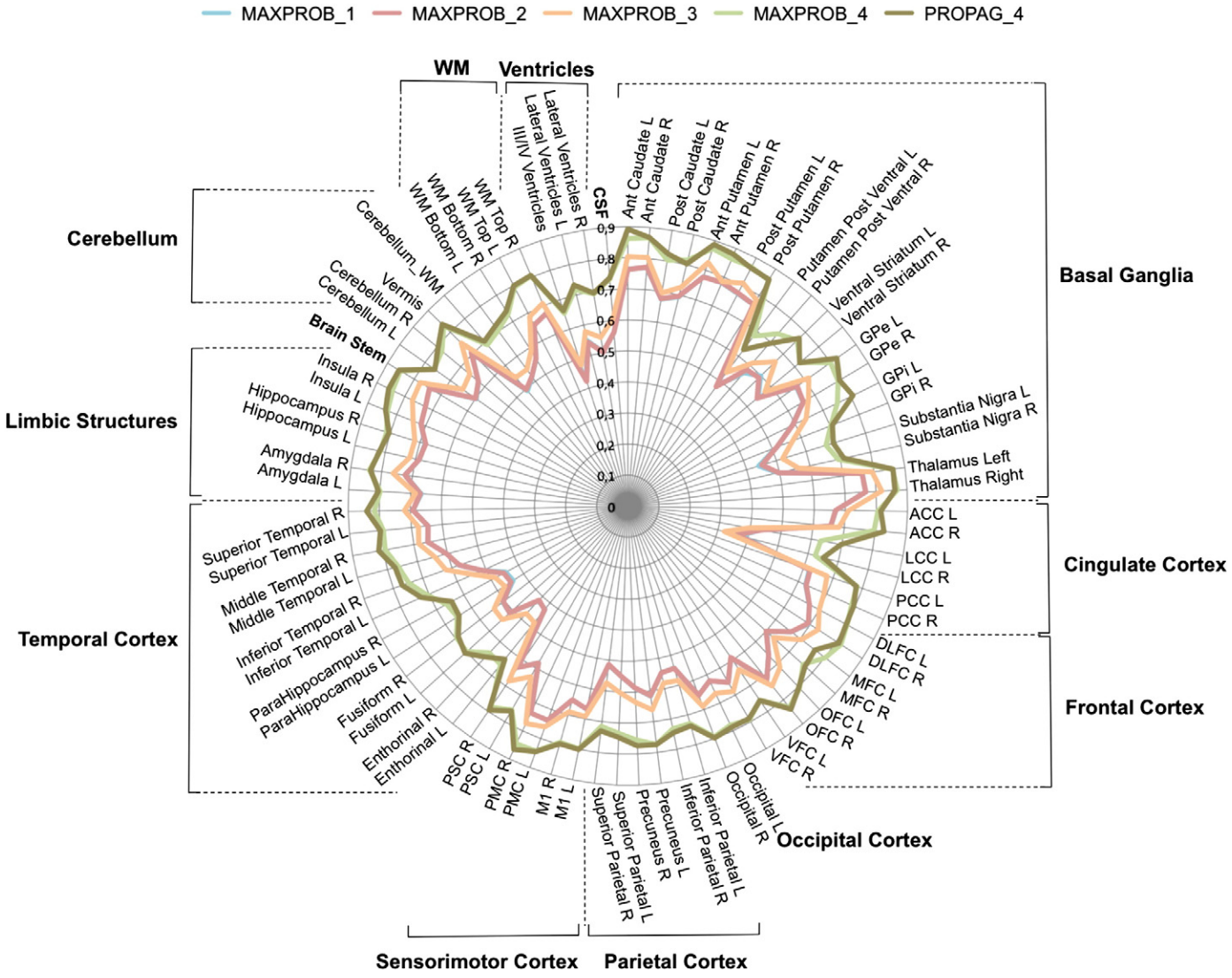

Fig. 7. Polar plot representation mean similarity index (Dice) between the manual delineation of brain structures, and their automated segmentation. SI are computed across anatomical regions (Table 1). MAXPROB_1 and MAXPROB_2 are superimposed.

close to 0.8 (Figs. 6 and 7) with no significant differences between the two automated segmentation methods. In parallel, we did not find any association between ROI volume and the overlap index. Our interpretation of these results is that four individual atlases are needed, for both automated methods, to reach the same accuracy of delineation as manual segmentation. No previous performance with the multi-atlas approach is available in the literature on non-human primates.

As a comparison, studies on humans (Gousias et al., 2008; Jia et al., 2012) showed that for a similar methodology (multi-atlas with affine transformation and maximum probability decision fusion), a performance of 0.8 was standard.

A limitation of the current study is that the volumetric measurement evaluation was performed on healthy cases. Inter-individual variability of structures is therefore limited to the control population. A study of pathological cases that may result in morphological modifications (such as lesions, grafts…) would need a preliminary validation and perhaps method improvement. As showed by McLaren et al. (2010), in a systematic comparison of normalisation procedure, the choice of the method for co-registering images is crucial. In addition, work in human multi-atlas showed that segmentation performances can be increased by the introduction of non-linear registrations with large degree of freedom (Heckemann et al., 2010; Jia et al., 2012), more sophisticated fusion rules (Gousias et al., 2008; Rohlfing et al., 2004) and an atlas selection procedure (Aljabar et al., 2009; Mallar Chakravarty et al., 2012). For example, we did not use a deformable model for image registration. Volumetric measurements made with an automated method would be more accurate if a non-linear registration method were used, which would certainly be necessary in studies of lesioned cases.

Accuracy of functional quantification

Our results showed that the modelling of binding parameters using automated methods was highly congruent with modelling using a manual delineation. Since modelling uses reference tissue, it requires an accurate extraction of the kinetics of the target region, as well as an accurate extraction of the reference region. Our validation showed that the extraction of time activity curves (TAC) with multi-atlas based segmented ROI was equivalent to TAC extraction with manual delineated regions.

The scatter plots clearly show that the BP_{ND} computed with automated methods is closely correlated with BP_{ND} computed using manual delineation. There is a noticeable reduction of the dispersion when using the PROPAG method, in comparison with the MAXPROB method,

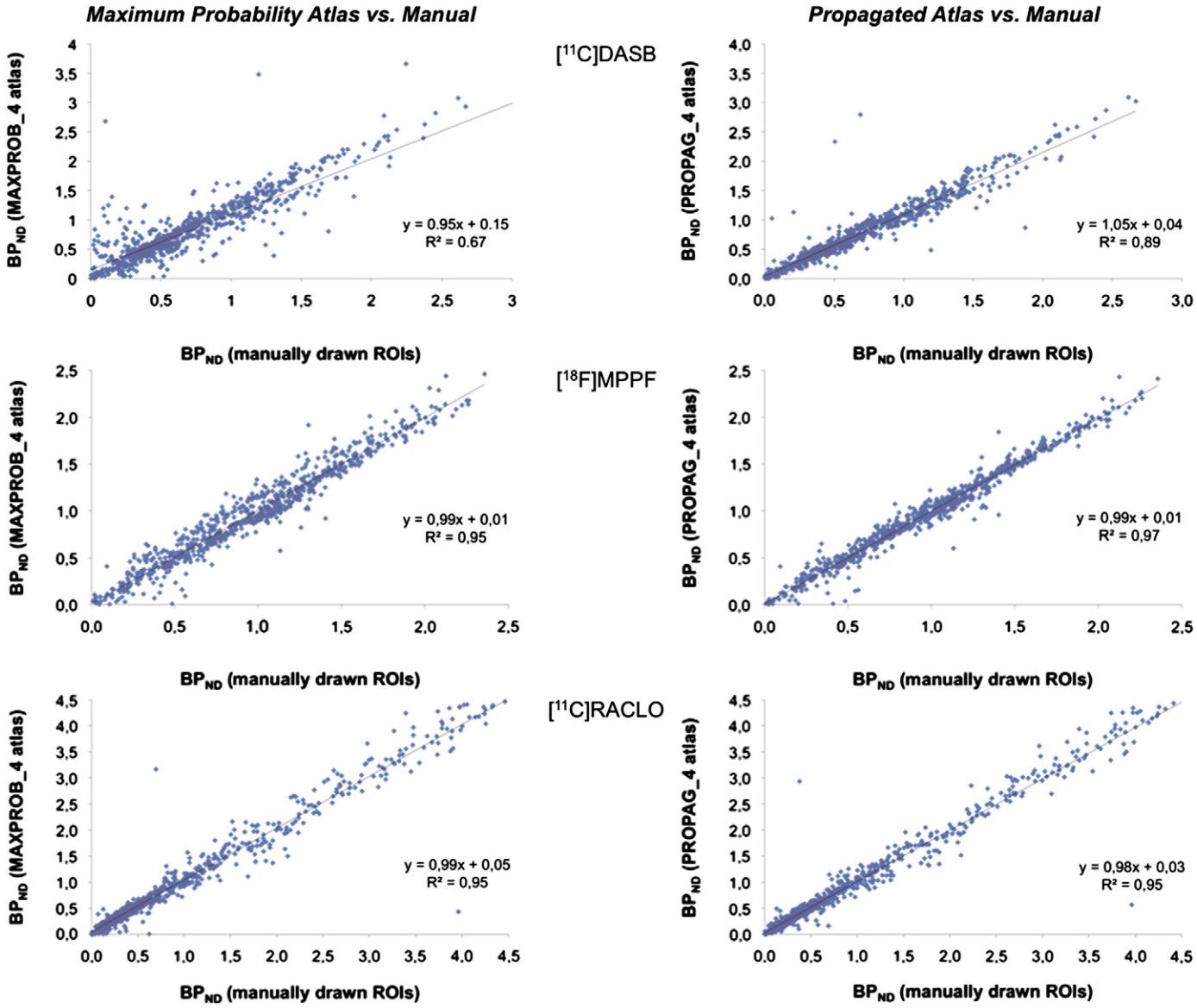

Fig. 8. Regression graphs of data from [^{11}C]DASB (N = 11), [^{18}F]MPPF (N = 10), and [^{11}C]Raclopride (N = 13) studies obtained from individual ROIs and from ROIs derived from MAXPROB_4 atlas (left column) and the PROPAG_4 atlas (right column). Linear regression curve equation and coefficient of correlation are given pooling data from the four individuals.

especially for tracers that bind the cortical structures. This is visible on the [^{11}C]DASB scatter plots and to a lesser extent for the [^{18} F]MPPF, which is a little more specific to the limbic system. Study of the [^{11}C] Raclopride, a selective tracer of the basal ganglia D2/D3 receptors, did not significantly benefit from the PROPAG method compared to the MAXPROB method. Nevertheless, none of the paired t-tests between automated and manual binding parameter extractions were significant. Altogether, these findings validate the use of multi-atlas segmentation for regional binding parameter computation.

Reproducibility

In this study we evaluated the reproducibility of the regional binding parameter estimation. This included an evaluation of the variability (bias and coefficient of variation), which represents the experimental and the biological errors of the measurement. Knowledge of measurement errors is essential to predict the statistical power of a design study, including the computation of the sample size needed to detect a significant variation between two groups or between two conditions in the same group (Costes et al., 2007). This variability and standard error highly depends on the methodology used for parameter estimation. Our study validates the use of automated methods that have the reproducibility of the manual method. Moreover, it shows that multi-atlas based segmentation reduces the standard error. With the MAXPROB_4 method, reproducibility was lower, ranging from 0.58 to 0.91, and with more variability, ranging from 8.2 to 19.2. The PROPAG_4 method reduced the spread of measurement. Indeed, the variability of the reproducibility was halved with this method, compared to the maximum probability method. The second parameter evaluated in the reproducibility study was the interclass coefficient. This parameter evaluated if the variability of a test –retest measurement was negligible with regard to inter-individual variability. A high ICC means that the test –retest reproducibility and the standard error of the measurement are negligible compared to the biological natural variability of the phenomenon. In our reproducibility study, we showed that an ICC over 0.6 with the MAXPROB method reached the level of .8 and even 0.97 with the PROPAG method. These latest results, which are close to the maximal value of 1, definitively validate the fact that automated methods

Table 4
Non-displaceable binding potentials (BP_{ND}) computed with manual, maximum probability (MAXPROB_4) or propagated (PROPAG_4) atlases for the [^{18}F]MPPF, and for the [^{11}C] Raclopride studies, in "control" conditions. *Bias* and *SD Bias* give the bias and the standard deviation of the bias of the BP_{ND} computed with the automated extraction versus the manual extraction. *Intra-class correlation coefficient* (ICC) gives the reproducibility of the BP_{ND} between manual and automated methods of extraction. Grey cells indicate the values where the PROPAG_4 method is significantly better that the MAXPROB_4 method.

		Manual	Maximum probability atlas (MAXPROB_4)				Propagated atlas (PROPAG_4)			
Ligand	Region	BP_{ND} (mean ± SD)	BP_{ND} (mean ± SD)	Bias (%)	SD Bias (%)	ICC	BP_{ND} (mean ± SD)	Bias (%)	SD Bias(%)	ICC
[^{18}F]MPPF	Amygdala	1.23 ± 0.25	1.22 ± 0.20	1.3	16.5	0.75	1.21 ± 0.24	-0.9	8.4	0.92
	Hippocampus	1.48 ± 0.34	1.47 ± 0.36	-0.4	14.0	0.74	1.43 ± 0.35	-3.0	9.0	0.88
	Enthorinal cortex	1.12 ± 0.09	1.15 ± 0.11	2.9	8.2	0.91	1.14 ± 0.10	1.9	5.8	0.95
	Anterior cingulate cortex	1.60 ± 0.36	1.65 ± 0.29	5.8	16.6	0.69	1.65 ± 0.30	4.5	8.2	0.91
	Frontal cortex	1.21 ± 0.32	1.22 ± 0.28	1.9	9.7	0.88	1.19 ± 0.31	-1.1	6.7	0.94
	Occipital cortex	0.41 ± 0.11	0.39 ± 0.06	-0.2	19.2	0.58	0.40 ± 0.09	-0.3	9.3	0.88
	Parietal cortex	1.09 ± 0.25	1.08 ± 0.20	0.7	12.7	0.77	1.09 ± 0.23	1.2	7.3	0.92
	Posterior cingulate cortex	1.33 ± 0.19	1.34 ± 0.08	2.2	10.2	0.81	1.33 ± 0.14	1.0	4.8	0.96
	Temporal cortex	0.81 ± 0.23	0.79 ± 0.23	-1.5	12.2	0.87	0.82 ± 0.23	1.1	6.4	0.97
[^{11}C]Raclo	Whole striatum	2.85 ± 0.88	2.88 ± 0.94	0.5	10.4	0.95	2.85 ± 0.92	-0.5	9.2	0.96
	Anterior caudate nucleus	3.03 ± 0.78	3.03 ± 0.85	-0.7	4.2	0.99	3.04 ± 0.88	-0.8	8.4	0.97
	Posterior caudate nucleus	2.86 ± 0.52	2.89 ± 0.76	-0.3	13.8	0.86	2.78 ± 0.67	-3.5	11.9	0.88
	Anterior putamen	3.21 ± 0.46	3.23 ± 0.56	0.5	6.5	0.96	3.20 ± 0.44	-0.1	4.3	0.98
	Posterior putamen	3.81 ± 0.22	3.87 ± 0.33	1.6	6.3	0.98	3.83 ± 0.32	0.7	6.5	0.98
	Ventral posterior putamen	2.31 ± 1.10	2.27 ± 1.07	-0.7	16.4	0.93	2.26 ± 1.10	-2.3	12.2	0.96
	Ventral striatum	1.90 ± 0.45	1.96 ± 0.58	2.8	11.8	0.83	1.96 ± 0.57	2.8	10.1	0.87

provide a reliable way of evaluating regional PET binding parameters. These findings are particularly evident with PET tracers that bind to the cortex such as, here, the [^{18}F]MPPF. In fact, for tracers of specific subcortical structures, such as the [^{11}C]Raclopride, the reliability of the functional quantification with the MAXPROB_4 method was high (around 10%) and this result was not improved by the PROPAG_4 method.

Rationale for the multi-subject atlas method

In the present study, we introduced, created and validated a multi-atlas based automated segmentation method. With this approach, the atlas does not rely on the anatomy of a single subject, but instead depends on nonlinear normalisation of numerous cynomolgus monkey brains mapped to an average MRI template image that is faithful to the location of anatomical structures. Combining information from multiple sources can compensate for the potential bias introduced by using a single atlas. The multi-atlas approach yields greater accuracy (Collins and Pruessner, 2010). In this study, each atlas consisted of 42 anatomical ROIs, which, together, covered the whole brain, brainstem and cerebellum as well as ventricles, white matter and cerebrospinal fluid. Although the delineation of the ROIs was operator-dependent and may be subjective, a detailed delineation protocol along the three orthogonal planes was used to define consistent and precise delineations (see Appendix A).

Both morphometric and functional evaluations showed that performances were increased with a multi-subject atlas, and specifically, that maximal performances were reached with four individual atlases.

Use of the MRI template and the maximum probability atlas in a reference space

We demonstrated the usefulness of a *M. fascicularis* brain template and its associated ROIs atlas to spatially normalise and quantify PET studies in a fully automated way. Indeed, our work allows the spatial normalisation of a dataset in the same reference space and thus allows voxel-by-voxel statistical analysis to be performed, as is widely done in human PET analysis, using, for instance, statistical parametric mapping (SPM) (Friston et al., 1994). Indeed, our ROIs atlas can be used to align many individual monkeys to carry out voxel-based analyses of multi-subject parametric images (Ashburner et al., 1998; Friston et al., 1999). The maximum probability atlas in the reference space may also be used for anatomical localization of a cluster of interest issuing from an SPM, for functional connectivity analysis of inter-regional activations, and for voxel-based morphometry analyses

Finally, the multi atlas-segmentation method will allow functional quantification to give an accurate regional value and/or kinetic extraction, which would take into account the individual neuroanatomical variability. In addition, accurate segmentation of the brain and the surrounding structures is appropriate for processing partial volume effect correction, for example with the GTM method (Rousset et al., 2008). Implementing automated segmentation for morphometric volumetric analysis might be further extended to pathological cases after introduction of non-linear registration methods, as has already been done in humans (Heckemann et al., 2011; Keihaninejad et al., 2012).

In conclusion, we obtained and validated a brain *M. fascicularis* template and its reference atlas for use as targets of automatic, voxel-based image registration methods. These new ROIs atlas address unmet needs for neuroimaging research in non-human primates. To our knowledge, this is the first approach that incorporates a large number of ROIs in an automatic anatomical segmentation method applicable to the *M. fascicularis* population. We demonstrated the adequacy and practical usefulness of the constructed template and the corresponding atlas. We believe the availability of these references will be helpful for future intra- and inter-individual voxel-based, longitudinal and multi-tracer analyses, and will facilitate analysis of neuroimaging studies in *M. fascicularis*.

By considering the multi-atlas set, the preliminary definition of an imaging protocol will have to consider the degree of accuracy of extracted parameters. Functional imaging studies that do not assess morphologic variation will not require an individual MRI for a tracer specific to a subcortical structure. Indeed, we showed that this economic choice would not affect the performance or the statistical power of the study. However, for a tracer known to bind a cortical structure, an accurate procedure for regional binding parameter extraction will require an individual MRI. By keeping this in mind, the methodological approach of the two automated techniques differed in one major aspect: automated segmentation with the propagated atlas needs an MRI of the subject, whereas automated segmentation with the maximum probability atlas does not.

Acknowledgements

We gratefully thank the radiochemistry team in the CERMEP, Frédéric Bonnefoi, Marion Malleval-Alvarez, the cyclotron operator, Christian Tourvielle, and the MRI staff, Jean-Christophe Comte and

Fabienne Vey. We thank Vincent Leviel for providing MRI scans. Valuable help was provided by Alexander Hammers and Rolf Heckemann. This work was supported by the French National Agency of Research (grant number ANR-09-MNPS-018).

Appendix A. Delineation protocol

Each region is defined in terms of its defining boundaries in each dimension according to Martin and Bowden's nomenclature (1996). When this is insufficient, footnotes are used.

Labels 1 and 2
Anterior Caudate Nucleus (right, left).

Orientation of slices	Coronal
Anterior border	Start on first slice on which caudate nucleus is visible at the lateral border of the lateral ventricle
Posterior border	Last slide on which the anterior commissure is completely visualised
Medial border	Lateral ventricle
Superior border	WM
Lateral border	WM
Inferior border	Anterior → Posterior: WM, Ventral Striatum, WM
Number of slices	~15

Labels 3 and 4
Anterior Putamen (right, left).

Orientation of slices	Coronal
Anterior border	Most anterior slice where putamen is seen
Posterior border	Last slide on which the anterior commissure is completely visualised
Medial border	Anterior → Posterior: Internal capsule/Ventral Striatum, External pallidum
Lateral border	WM (External capsule)
Superior border	WM
Inferior border	WM
Number of slices	~12

Labels 5 and 6
Ventral Striatum (right, left).

Include inferior part of the anterior striatum, accumbens nucleus and substantia innominata.	
Orientation of slices	Coronal; start posteriorly
Anterior border	Last slice where ventral striatum can be clearly differentiated from the anterior caudate nucleus (e.g. inferior part of the anterior caudate visible)
Posterior border	First slice after the anterior commissure is fully visible
Medial border	Lateral ventricle, WM
Lateral border	WM
Superior border	Anterior striatum (Ventral striatum is always inferior to lateral ventricle)
Inferior border	Anterior → Posterior: WM, Anterior Commissure
Number of slices	~15

Labels 7 and 8
External Pallidum (right, left).

Orientation of slices	Coronal
Anterior border	First slice on which the anterior commissure is completely visualised
Posterior border	Last slice where visible
Medial border	Anterior → Posterior: WM, Internal pallidum, WM
Lateral border	Putamen
Superior border	Internal capsule
Inferior border	Anterior → Posterior: WM, Ventral posterior putamen, WM
Number of slices	~13

Labels 9 and 10
Internal Pallidum (right, left).

Orientation of slices	Coronal
Anterior border	Start on first slice on which the frontal horn of the lateral ventricle and the third ventricles are joined.
Posterior border	Last slice where visible
Medial border	WM
Lateral border	External pallidum
Superior border	Internal capsule (Line drawn by the superior borders of posterior putamen and external pallidum)
Inferior border	WM (Horizontal line drawn by inferior borders of posterior putamen and external pallidum)
Number of slices	~8

Labels 11 and 12
Posterior Caudate Nucleus (right, left).

Orientation of slices	Coronal
Anterior border	Anterior caudate nucleus
Posterior border	Last slice where visible
Medial border	Lateral ventricle
Lateral border	WM
Superior border	WM
Inferior border	Anterior → Posterior: WM, Thalamus, WM
Number of slices	~21

Labels 13 and 14
Posterior Putamen (right, left).

Orientation of slices	Coronal
Anterior border	Anterior putamen
Posterior border	Last slice where visible
Medial border	Anterior → Posterior: External pallidum, WM
Lateral border	WM (external capsule)
Superior border	WM
Inferior border	Anterior → Posterior: WM, ventral posterior putamen, WM
Number of slices	~19

Labels 15 and 16
Ventral Posterior Putamen (right, left).

Orientation of slices	Coronal
Anterior border	Start on first slice on which the third ventricle is discontinued
Posterior border	Last slice where visible
Medial border	WM
Lateral border	WM
Superior border	Inferior borders of posterior putamen and external pallidum
Inferior border	WM
Number of slices	~12

Caution: Use sagittal orientation for help with superior, lateral and inferior borders.

Labels 17 and 18
Substantia Nigra (right, left).

Orientation of slices	Coronal
Anterior border	Level of the mamillary bodies
Posterior border	Last slide where visible
Medial border	Brain Stem
Lateral border	Brain Stem
Superior border	Brain Stem
Inferior border	Brain Stem
Number of slices	~10

Caution: Use transverse orientation initially to aid the delineation of the structure where the nigra is clearly visible in its entire anteroposterior extent.

Labels 19 and 20
Thalamus (right, left).

Orientation of slices	Coronal
Anterior border	Start on first slice on which the third ventricle is discontinued
Posterior border	Last slice where visible
Medial border	Midline/Third ventricle
Lateral border	WM
Superior border	WM then more posteriorly draw an horizontal line following the inferior borders of lateral ventricle
Inferior border	Anterior → Posterior: WM, Brain Stem, WM
Number of slices	~15

Caution: The use of the mid-sagittal slices facilitated more accurate determination of the different borders. In addition use the transverse orientation for help with lateral borders.

Labels 21 and 22
Hippocampus (right, left).

Orientation of slices	Coronal
Anterior border	Start on first slice where the internal pallidum begins (as previously defined, see Labels 9 and 10).
Posterior border	Most posterior slice where the body and the temporal horn of lateral ventricle fuse, before the occipital horn of lateral ventricle begins
Medial border	Anterior → Posterior: Enthorinal area, CSF, Parahippocampal gyrus; WM
Lateral border	Anterior → Posterior: WM, Lateral Ventricle
Superior border	Anterior → Posterior: Amygdala, WM, and CSF
Inferior border	Anterior → Posterior: Enthorinal area, WM
Number of slices	~27

Labels 23 and 24
Amygdala (right, left).

Include prepyriform and periamygdaloid areas, amygdala, basolateral nuclear group, basal and cortical amygdaloid nuclei.	
Orientation of slices	Coronal
Anterior border	Start on first slide on which the rhinal sulcus is visible
Posterior border	Most posterior slice before thalamus appears (as previously defined, see Labels 19 and 20)
Medial border	CSF
Lateral border	Anterior → Posterior: Superior temporal gyrus, WM
Superior border	Anterior → Posterior: CSF, WM
Inferior border	Anterior → Posterior: CSF, Middle temporal gyrus, Enthorinal area, Hippocampus
Number of slices	~14

Labels 27 and 28
Insula (right, left).

Orientation of slices	Coronal
Anterior border	First slice on which insular sulcus is visualised
Posterior border	Last slice on which insular sulcus is visualised
Medial border	WM (Lateral edge of the extreme or external capsule)
Lateral border	CSF within lateral sulcus
Superior border	Insular sulcus
Inferior border	Insular sulcus
Number of slices	~26

Caution: Start by estimating anterior–posterior and superior–inferior extent with sagittal slices when the insular sulcus is completely visible.

Labels 29 and 30
Cerebellum (right, left).

Orientation of slices	Sagittal
Anterior border	First slice on which the cerebellar peduncle joins the brainstem
Posterior border	CSF
Medial border	Vermis (see structure 72)
Lateral border	CSF
Superior border	CSF
Inferior border	CSF
Number of slices	~34

Labels 31 and 32
Orbitofrontal Cortex (right, left).

Include gyrus rectus; medial, lateral, and fronto-orbital gyri.	
Orientation of slices	Coronal
Anterior border	CSF
Posterior border	End one slice before insula appears (as previously defined, see Labels 27 and 28)
Medial border	Midline
Lateral border	Anterior → Posterior: CSF, Precentral Gyrus, WM
Superior/lateral border	Anterior → Posterior: Inferior frontal gyrus, WM, Extreme capsule
Superior/medial border	Anterior → Posterior: Superior frontal gyrus, Anterior cingulate gyrus/Rostral sulcus
Inferior border	CSF
Number of slices	~36

Labels 33 and 34
Anterior Cingulate Cortex (right, left).

Orientation of slices	Sagittal then coronal
Sagittal cuts	
Anterior border	Cingulate sulcus
Posterior border	Draw a vertical line from corpus callosum to cingulate sulcus at the mid-point of the greatest extension of the corpus callosum on most medial slice; corpus callosum inferiorly
Medial border	Midline
Lateral border	Last slice on which cingulate sulcus is visible in its full length (then change to coronal cuts)
Superior border	Cingulate sulcus
Coronal cuts	
Anterior border	As previously defined on sagittal cuts
Posterior border	As previously defined on sagittal cuts
Medial border	As previously defined on sagittal cuts
Lateral border	WM
Superior border	As previously defined on sagittal cuts
Inferior border	Anterior → Posterior: Gyrus rectus, Rostral sulcus, Callosal sulcus
Number of slices	~38

Labels 35 and 36
Limbic Cingulate Cortex (right, left).

Orientation of slices	Coronal
Anterior border	First slice when the genu of corpus callosum appears
Posterior border	End when insular sulcus is visible
Medial border	Midline
Lateral border	WM
Superior border	Corpus Callosum
Inferior border	Anterior → Posterior: Rostral sulcus, Gyrus rectus
Number of slices	~6

Labels 37 and 38
Posterior Cingulate Cortex (right, left).

Orientation of slices	Coronal
Anterior border	Anterior cingulate cortex
Posterior border	Subparietal sulcus (mid-sagittal orientation)
Medial border	Midline
Lateral border	WM
Superior border	Anterior → Posterior: Cingulate sulcus, Precuneus, Subparietal sulcus
Inferior border	Anterior → Posterior: Callosal sulcus, Cuneus
Number of slices	~34

Labels 39 and 40
Dorsolateral frontal Cortex (right, left).

Include superior and middle frontal gyri.	
Orientation of slices	Coronal
Anterior border	CSF
Posterior border	Last slice = last slice where the principal sulcus is visible
Medial border	Anterior → Posterior: Superior frontal gyrus (medial part), Superior ramus of arcuate sulcus
Lateral border	CSF
Superior border	CSF
Inferior border	Principal sulcus
Number of slices	~32

Labels 41 and 42
Parahippocampal Gyrus (right, left).

Orientation of slices	Coronal
Anterior border	Start on first slice on which rhinal sulcus is no longer visible
Posterior border	Posterior border of the hippocampus as previously defined (that slice included, see Labels 21 and 22)
Medial border	CSF
Lateral/Superior border	Anterior → Posterior: Hippocampus, WM
Lateral/Inferior border	Fusiform gyrus
Superior border	Anterior → Posterior: Hippocampus, CSF
Inferior border	CSF
Number of slices	~20

Labels 43 and 44
Superior Temporal Cortex (right, left).

Orientation of slices	Coronal
Anterior border	CSF
Posterior border	End when the lateral sulcus is no longer visible
Medial Border	Anterior → Posterior: CSF, Rhinal Sulcus, WM, Insular sulcus, WM
Lateral border	CSF
Superior border	Anterior → Posterior: CSF, Lateral sulcus
Inferior border	Anterior → Posterior: CSF, Superior temporal sulcus
Number of slices	~56

Labels 45 and 46
Medial Temporal Cortex (right, left).

Orientation of slices	Coronal
Anterior border	Locate the first slice on which the superior temporal as well as the rhinal sulci are visible. Then draw horizontal line between both.
Posterior border	End one slide before inferior occipital sulcus appears
Medial Border	Anterior → Posterior: CSF, Inferior temporal gyrus, Anterior middle temporal sulcus, WM
Lateral border	CSF
Superior border	Superior temporal sulcus
Inferior border	Anterior → Posterior: CSF, Inferior temporal gyrus
Number of slices	~45

Labels 47 and 48
Inferior Temporal Cortex (right, left).

Orientation of slices	Coronal
Anterior border	Start on the slide where insula appears (as previously defined, see Labels 27 and 28)
Posterior border	Posterior border of the medial temporal cortex (as previously defined, see Labels 45 and 46)
Medial border	Anterior → Posterior: CSF, rhinal sulcus, Fusiform gyrus, Occipito-temporal sulcus
Lateral border	Anterior → Posterior: WM, Middle temporal gyrus, Anterior middle temporal sulcus, Middle temporal gyrus
Superior border	Anterior → Posterior: Rhinal sulcus, middle temporal sulcus, WM
Inferior border	Anterior → Posterior: Middle temporal gyrus, CSF
Number of slices	~43

Labels 49 and 50
Occipital Cortex (right, left).

Include inferior occipital gyrus, lingual gyrus, cuneus and occipital gyrus	
Orientation of slices	First sagittal, then transverse
Sagittal cuts (start medially)	
Anterior border	Parieto-occipital sulcus
Posterior border	CSF
Medial border	Midline
Lateral border	Last slice on which parieto-occipital sulcus is visible in its full length (then change to transverse cuts)
Superior border	Parieto-occipital sulcus/CSF
Inferior border	CSF (Cerebellar tentorium)
Transverse cuts	
Anterior border	Straight line between medial end of anterior occipital sulcus, and lateral end of parieto-occipital sulcus
Posterior border	As previously defined on sagittal cuts
Medial border	As previously defined on sagittal cuts
Lateral border	CSF
Superior border	Anterior occipital sulcus
Inferior border	As previously defined on sagittal cuts
Number of slices	~39 (coronal)

Labels 51 and 52
Superior Parietal Cortex.

Orientation of slices	Coronal
Anterior border	Start when the putamen posterior ventral is no longer visible (as previously defined, see Labels 15 and 16)
Posterior border	Last slide where the intraparietal sulcus is visible; CSF
Medial border	Anterior → Posterior: WM, Midline, Cingulate sulcus, Precuneus
Lateral border	Anterior → Posterior: CSF, Intraparietal sulcus
Superior border	Anterior → Posterior: Postcentral gyrus, Superior postcentral sulcus, CSF
Inferior border	Anterior → Posterior: Intraparietal sulcus, Cingulate sulcus, Simian fossa, WM
Number of slices	~34

Caution: The use of the sagittal and transverse slices facilitates more accurate determination of the different borders on slices where the intraparietal sulcus is clearly visible.

Labels 53 and 54
Inferior Parietal Cortex (right, left).

Include the angular and supramarginal gyri.	
Orientation of slices	Coronal
Supramarginal gyrus	
Anterior border	Start on first slide on which intraparietal sulcus is clearly visible
Medial border	WM
Lateral border	CSF
Superior border	Intraparietal sulcus
Inferior border	Lateral sulcus
Angular gyrus	
Anterior border	Start on first slide on which inferior occipital sulcus is visible
Medial border	WM
Lateral border	CSF
Superior border	Superior temporal sulcus
Inferior border	Inferior occipital sulcus
Then when the lateral sulcus is no longer visible the supramarginal and angular gyri fuse.	
Posterior border	End when intraparietal and lunate sulci disappear.
Medial border	Anterior → Posterior: WM, Intraparietal sulcus
Lateral border	CSF
Superior border	Anterior → Posterior: Intraparietal sulcus, CSF
Inferior border	Anterior → Posterior: Inferior occipital sulcus, lunate sulcus, simian fossa
Number of slices	~35

Labels 55 and 56
Precuneus (right, left).

Orientation of slices	Coronal then transverse
Coronal cuts	
Anterior border	First slide = Last slide where the splenium of corpus callosum is visible
Posterior border	Last slide where the intraparietal sulcus is visible
Transverse cuts	
Medial border	Midline
Lateral border	WM
Sup/Ant. border	Cingulate sulcus
Sup/Post. border	Superior→ Inferior: Superior parietal cortex, CSF, Occipital Cortex
Inf./Ant. border	Anterior parieto-occipital sulcus
Inf./Post. border	Parieto-occipital sulcus
Number of slices	~24 (coronal)

Labels 57 and 58
Premotor Cortex (right, left).

Include superior frontal gyrus (dorsal part) and precentral gyrus (ventral part)	
Orientation of slices	Coronal
Dorsal premotor cortex	
Anterior border	Start on first slide on which genu of corpus callosum appears
Medial border	Midline
Superior border	CSF
Inf./Med. border	Cingulate sulcus
Inf./Lat. Border	Superior ramus of arcuate sulcus
Ventral premotor cortex	
Anterior border	Start on first slide on which inferior ramus of arcuate sulcus is visible
Medial border	Fronto-orbital gyrus
Lateral border	CSF
Superior border	Inferior ramus of arcuate sulcus
Inferior border	Anterior → Posterior: CSF, Lateral sulcus
Then dorsal and ventral premotor parts join when the principal sulcus is no longer visible	
Posterior border	End one slice before the central sulcus appears
Medial border	Midline
Lateral border	CSF
Superior border	CSF
Inf./Med. border	Cingulate sulcus
Inf./Lat. Border	Anterior → Posterior: Insular sulcus, Anterior subcentral sulcus, Superior arcuate sulcus
Number of slices	~27

Labels 59 and 60
Primary Motor Cortex (right, left).

Orientation of slices	Transverse then coronal
Transverse cuts	
Anterior border	Posterior border of the premotor cortex
Posterior border	Central sulcus
Coronal cuts	
Medial border	Anterior → Posterior: WM, Midline
Lateral border	CSF
Superior border	Anterior → Posterior: Superior arcuate sulcus, CSF
Inf./Lat. border	Central sulcus
Inf./Med. border	Cingulate sulcus
Number of slices	~25 (coronal)

Caution: Use transverse orientation to help delineate the posterior border along the central sulcus.

Labels 61 and 62
Primary Sensory Cortex (right, left).

Orientation of slices	Coronal
Start anteriorly with the lateral part of the structure	
Anterior border	Same level that putamen posterior (as previously defined, see Labels 13 and 14)
Medial border	Anterior → Posterior: Insular sulcus, Central sulcus
Lateral border	CSF
Superior border	Anterior → Posterior: Anterior subcentral sulcus, Central sulcus, CSF
Inferior border	Anterior → Posterior: Lateral sulcus, Intraparietal sulcus, Superior parietal cortex
When the intraparietal sulcus begins start to draw the medial part of the structure	
Medial border	Midline
Lateral border	WM
Superior border	Primary motor cortex
Inferior border	Cingulate sulcus
Then when central sulcus is no longer visible the lateral and medial parts of the primary sensory cortex fuse	
Posterior border	End when the superior postcentral sulcus is no longer visible
Number of slices	~33

Caution: Use transverse orientation to help delineate the anterior border along the central sulcus.

Labels 63 and 64
Ventral frontal Cortex (right, left).

Include Inferior and middle frontal gyri.	
Orientation of slices	Coronal
Anterior border	CSF
Posterior border	End when the principal sulcus is no longer visible
Medial border	WM
Lateral border	CSF
Superior border	Principal sulcus/CSF
Inferior border	Anterior → Posterior: Fronto-Orbital gyrus/CSF, Inferior ramus of arcuate sulcus
Number of slices	~32

Labels 65 and 66
Fusiform Gyrus (right, left).

Orientation of slices	Coronal
Anterior border	Start on first slice on which parahippocampal gryus is visualised (as previously defined, see Labels 41 and 42)
Posterior border	Last slide where occipito-temporal sulcus is visible
Medial border	Anterior → Posterior: Parahippocampal gyrus, Collateral sulcus
Lateral border	Anterior → Posterior: Inferior temporal gyrus, Occipito-temporal sulcus
Superior border	WM
Inferior border	CSF
Number of slices	~45

Labels 67 and 68
Enthorinal Cortex (right, left).

Orientation of slices	Coronal
Anterior border	Start on first slice on which insula begins (as previously defined, see Labels 27 and 28)
Posterior border	Anterior border of parahippocampal and fusiform gyri as previously defined (see Labels 41 and 42 and 65 and 66 respectively)
Medial border	CSF
Lateral border	Anterior → Posterior: WM, Hippocampus
Superior border	Anterior → Posterior: Amygdala, Hippocampus
Inferior border	Anterior → Posterior: Inferior temporal cortex, CSF
Number of slices	~15

Labels 69 and 70
Medial frontal Cortex (right, left).

Orientation of slices	Coronal
Anterior border	CSF
Posterior border	End one slide before the genu of corpus callosum is visualised
Medial border	Midline
Lateral border	Anterior → Posterior: Dorsolateral frontal cortex, WM
Superior border	CSF
Inferior border	Anterior → Posterior: Gyrus rectus, Cingulate sulcus
Number of slices	~23

Label 72
Vermis.

Orientation of slices	Coronal
Anterior border	Begin at the cerebellum mid-sagittal slice
Posterior border	Cerebellum
Medial border	Midline
Lateral border	CSF
Superior border	CSF
Inferior border	CSF
Number of slices	~33

Labels 80 and 81
White Matter, top part (right, left).

Include corpus callosum, internal capsule, external capsule, extreme capsule	
Orientation of slices	Transverse
Include all remaining area above the virtual horizontal line drawn by posterior borders of thalamus, posterior putamen and insula.	

Labels 82 and 83
White Matter, bottom part (right, left).

The remaining area after drawing the top part

Label 84
Brain Stem.

Orientation of slices	Sagittal
Anterior border	CSF
Posterior border	CSF
Medial border	No medial border, spans the midline
Lateral border	CSF
Superior border	Cut from basal ganglia as soon as pedunculus cerebri enters them using a tangential line following the contours of the basal ganglia.
Inferior border	Inferior border of the cerebellum
Number of slices	~32

Caution: Start at the mid-sagittal slice and work medial to lateral.

Labels 85 and 86
Lateral Ventricles (right, left).

Include frontal, body and occipital horns of the lateral ventricles.	
Orientation of slices	Coronal
Anterior border	Start on first slice on which frontal horn is visible
Posterior border	Last slide where the occipital horn of lateral ventricle is visible
Medial border	Anterior → Posterior: WM, Midline/Third ventricle
Lateral border	Anterior → Posterior: Anterior caudate nucleus, Ventral striatum, Posterior caudate nucleus
Superior border	WM
Inferior border	Anterior → Posterior: WM, Ventral striatum, WM (Anterior commissure), Third ventricle/WM, Thalamus, WM
Number of slices	~55

Label 87
Third and Fourth Ventricles.

Orientation of slices	Coronal
Third ventricle	
Anterior border	Lamina terminalis (CSF)
Posterior border	Pineal gland
Medial border	None (midline structures)
Lateral border	Anterior → Posterior: WM, Thalamus, WM
Superior border	Fornix (WM)
Inferior border	Anterior → Posterior: Optic chiasma, WM
Fourth ventricle	
Anterior border	First slice on which the fourth ventricle is seen between the brain stem and cerebellum
Posterior border	Last slide where visible
Medial border	None (midline structures)
Lateral border	Brain Stem
Superior border	Brain Stem
Inferior border	Brain Stem
Number of slices	~38

Label 88
Cerebellum White Matter.

The remaining area after drawing the cerebellum (grey matter) and the vermis	
Number of slices	~23 (coronal)

Label 89
Cerebrospinal Fluid.

The remaining area after drawing all the structures defined above

References

Aljabar, P., Heckemann, R.A., Hammers, A., Hajnal, J.V., Rueckert, D., 2009. Multi-atlas based segmentation of brain images: atlas selection and its effect on accuracy. NeuroImage 46, 726–738.

Ashburner, J., Hutton, C., Frackowiak, R., Johnsrude, I., Price, C., Friston, K., 1998. Identifying global anatomical differences: deformation-based morphometry. Hum. Brain Mapp. 6, 348–357.

Black, K.J., Gado, M.H., Videen, T.O., Perlmutter, J.S., 1997. Baboon Basal Ganglia Stereotaxy Using Internal MRI Landmarks: Validation and Application to PET Imaging. J. Comput. Assist. Tomogr. 21, 881.

Black, K.J., Koller, J.M., Snyder, A.Z., Perlmutter, J.S., 2001a. Template images for nonhuman primate neuroimaging: 2. Macaque. NeuroImage 14, 744–748.

Black, K.J., Snyder, A.Z., Koller, J.M., Gado, M.H., Perlmutter, J.S., 2001b. Template images for nonhuman primate neuroimaging: 1. Baboon. NeuroImage 14, 736–743.

Blesa, J., Pifl, C., Sánchez-González, M.A., Juri, C., García-Cabezas, M.A., Adánez, R., Iglesias, E., Collantes, M., Peñuelas, I., Sánchez-Hernández, J.J., Rodriguez-Oroz, M.C., Avendaño, C., Hornykiewicz, O., Cavada, C., Obeso, J.A., 2012. The nigrostriatal system in the presymptomatic and symptomatic stages in the MPTP monkey model: A PET, histological and biochemical study. Neurobiol. Dis. 48, 79–91.

Brix, G., Zaers, J., Adam, L.E., Bellemann, M.E., Ostertag, H., Trojan, H., Haberkorn, U., Doll, J., Oberdorfer, F., Lorenz, W.J., 1997. Performance evaluation of a whole-body PET scanner using the NEMA protocol. National Electrical Manufacturers Association. J. Nucl. Med. 38, 1614–1623.

Brown, C.A., Campbell, M.C., Karimi, M., Tabbal, S.D., Loftin, S.K., Tian, L.L., Moerlein, S.M., Perlmutter, J.S., 2012. Dopamine pathway loss in nucleus accumbens and ventral tegmental area predicts apathetic behavior in MPTP-lesioned monkeys. Exp. Neurol. 236, 190–197.

Collantes, M., Prieto, E., Peñuelas, I., Blesa, J., Juri, C., Martí-Climent, J.M., Quincoces, G., Arbizu, J., Riverol, M., Zubieta, J.L., Rodriguez-Oroz, M.C., Luquin, M.R., Richter, J.A., Obeso, J.A., 2009. New MRI, 18 F-DOPA and 11C-(+)-alpha-dihydrotetrabenazine templates for Macaca fascicularis neuroimaging: advantages to improve PET quantification. NeuroImage 47, 533–539.

Collins, D.L., Pruessner, J.C., 2010. Towards accurate, automatic segmentation of the hippocampus and amygdala from MRI by augmenting ANIMAL with a template library and label fusion. NeuroImage 52, 1355–1366.

Collins, D.L., Neelin, P., Peters, T.M., Evans, A.C., 1994. Automatic 3D intersubject registration of MR volumetric data in standardized Talairach space. J. Comput. Assist. Tomogr. 18, 192–205.

Costes, N., Zimmer, L., Reilhac, A., Lavenne, F., Ryvlin, P., Le Bars, D., 2007. Test–retest reproducibility of 18 F-MPPF PET in healthy humans: a reliability study. J. Nucl. Med. 48, 1279–1288.

Fox, P.T., Perlmutter, J.S., Raichle, M.E., 1985. A stereotactic method of anatomical localization for positron emission tomography. J. Comput. Assist. Tomogr. 9, 141–153.

Frey, S., Pandya, D.N., Chakravarty, M.M., Bailey, L., Petrides, M., Collins, D.L., 2011. An MRI based average macaque monkey stereotaxic atlas and space (MNI monkey space). NeuroImage 55, 1435–1442.

Friston, K.J., Holmes, A.P., Worsley, K.J., Poline, J.P., Frith, C.D., Frackowiak, R.S.J., 1994. Statistical parametric maps in functional imaging: A general linear approach. Hum. Brain Mapp. 2, 189–210.
Friston, K.J., Ashburner, J., Frith, C.D., Poline, J.B., Heather, J.D., Frackowiak, R.S.J., 1995. Spatial registration and normalization of images. Hum. Brain Mapp. 3, 165–189.
Friston, K.J., Holmes, A.P., Price, C.J., Buchel, C., Worsley, K.J., 1999. Multisubject fMRI studies and conjunction analyses. NeuroImage 10, 385–396.
Gousias, I.S., Rueckert, D., Heckemann, R.A., Dyet, L.E., Boardman, J.P., Edwards, A.D., Hammers, A., 2008. Automatic segmentation of brain MRIs of 2-year-olds into 83 regions of interest. NeuroImage 40, 672–684.
Greer, P.J., Villemagne, V.L., Ruszkiewicz, J., Graves, A.K., Meltzer, C.C., Mathis, C.A., Price, J.C., 2002. MR atlas of the baboon brain for functional neuroimaging. Brain Res. Bull. 58, 429–438.
Gunn, R.N., Laamerstma, A.A., Hume, S.P., Cunningham, V.J., 1997. Parametric imaging of ligand-receptor binding in PET using a simplified reference region. NeuroImage 6, 279–287.
Hammers, A., Koepp, M.J., Free, S.L., Brett, M., Richardson, M.P., Labbé, C., Cunningham, V.J., Brooks, D.J., Duncan, J., 2002. Implementation and application of a brain template for multiple volumes of interest. Hum. Brain Mapp. 15, 165–174.
Hammers, A., Allom, R., Koepp, M.J., Free, S.L., Myers, R., Lemieux, L., Mitchell, T.N., Brooks, D.J., Duncan, J.S., 2003. Three-dimensional maximum probability atlas of the human brain, with particular reference to the temporal lobe. Hum. Brain Mapp. 19, 224–247.
Heckemann, R.A., Hajnal, J.V., Aljabar, P., Rueckert, D., Hammers, A., 2006. Automatic anatomical brain MRI segmentation combining label propagation and decision fusion. NeuroImage 33, 115–126.
Heckemann, R.A., Keihaninejad, S., Aljabar, P., Rueckert, D., Hajnal, J.V., Hammers, A., Alzheimer's Disease Neuroimaging Initiative, 2010. Improving intersubject image registration using tissue-class information benefits robustness and accuracy of multi-atlas based anatomical segmentation. NeuroImage 51, 221–227.
Heckemann, R.A., Keihaninejad, S., Aljabar, P., Gray, K.R., Nielsen, C., Rueckert, D., Hajnal, J.V., Hammers, A., Alzheimer's Disease Neuroimaging Initiative, 2011. Automatic morphometry in Alzheimer's disease and mild cognitive impairment. NeuroImage 56, 2024–2037.
Hikishima, K., Quallo, M.M., Komaki, Y., Yamada, M., Kawai, K., Momoshima, S., Okano, H.J., Sasaki, E., Tamaoki, N., Lemon, R.N., Iriki, A., Okano, H., 2011. Population-averaged standard template brain atlas for the common marmoset (Callithrix jacchus). NeuroImage 54, 2741–2749.
Jia, H., Yap, P.-T., Shen, D., 2012. Iterative multi-atlas-based multi-image segmentation with tree-based registration. NeuroImage 59, 422–430.
Keihaninejad, S., Heckemann, R.A., Gousias, I.S., Hajnal, J.V., Duncan, J.S., Aljabar, P., Rueckert, D., Hammers, A., 2012. Classification and lateralization of temporal lobe epilepsies with and without hippocampal atrophy based on whole-brain automatic MRI segmentation. PLoS One 7, e33096.
Lanciego, J.L., Vázquez, A., 2011. The basal ganglia and thalamus of the long-tailed macaque in stereotaxic coordinates. A template atlas based on coronal, sagittal and horizontal brain sections. Brain Struct. Funct. 217, 613–666.
Mallar Chakravarty, M., Steadman, P., van Eede, M.C., Calcott, R.D., Gu, V., Shaw, P., Raznahan, A., Louis Collins, D., Lerch, J.P., 2012. Performing label-fusion-based segmentation using multiple automatically generated templates. Hum. Brain Mapp. http://dx.doi.org/10.1002/hbm.22092.
Martin, R.F., Bowden, D.M., 1996. A stereotaxic template atlas of the macaque brain for digital imaging and quantitative neuroanatomy. NeuroImage 4 (2), 119–150.
McLaren, D.G., Kosmatka, K.J., Oakes, T.R., Kroenke, C.D., Kohama, S.G., Matochik, J.A., Ingram, D.K., Johnson, S.C., 2009. A population-average MRI-based atlas collection of the rhesus macaque. NeuroImage 45, 52–59.
McLaren, D.G., Kosmatka, K.J., Kastman, E.K., Bendlin, B.B., Johnson, S.C., 2010. Rhesus macaque brain morphometry: a methodological comparison of voxel-wise approaches. Methods 50, 157–165.
Nagai, Y., Minamimoto, T., Ando, K., Obayashi, S., Ito, H., Ito, N., Suhara, T., 2012. Correlation between decreased motor activity and dopaminergic degeneration in the ventrolateral putamen in monkeys receiving repeated MPTP administrations: A positron emission tomography study. Neurosci. Res. 73, 54–60.
Neumane, S., Mounayar, S., Jan, C., Epinat, J., Ballanger, B., Costes, N., Féger, J., Thobois, S., François, C., Sgambato-Faure, V., Tremblay, L., 2012. Effects of dopamine and serotonin antagonist injections into the striatopallidal complex of asymptomatic MPTP-treated monkeys. Neurobiol. Dis. 48, 27–39.
NIH, 2011. Guide for the Care and Use of Laboratory Animals, eighth ed. National research Council of the National Academies.
Quallo, M.M., Price, C.J., Ueno, K., Asamizuya, T., Cheng, K., Lemon, R.N., Iriki, A., 2010. Creating a population-averaged standard brain template for Japanese macaques (M. fuscata). NeuroImage 52, 1328–1333.
Rilling, J.K., Barks, S.K., Parr, L.A., Preuss, T.M., Faber, T.L., Pagnoni, G., Bremner, J.D., Votaw, J.R., 2007. A comparison of resting-state brain activity in humans and chimpanzees. Proc. Natl. Acad. Sci. U. S. A. 104, 17146–17151.
Rohlfing, T., Brandt, R., Menzel, R., Maurer, C.R., 2004. Evaluation of atlas selection strategies for atlas-based image segmentation with application to confocal microscopy images of bee brains. NeuroImage 21, 1428–1442.
Rousset, O.G., Collins, D.L., Rahmim, A., Wong, D.F., 2008. Design and Implementation of an Automated Partial Volume Correction in PET: Application to Dopamine Receptor Quantification in the Normal Human Striatum. J. Nucl. Med. 49, 1097–1106.
Saleem, K.S., Logothetis, N.K., 2007. A Combined MRI and Histology Atlas of the Rhesus Monkey Brain in Stereotaxic Coordinates. Academic, London.
Smith, S.M., 2002. Fast robust automated brain extraction. Hum. Brain Mapp. 17, 143–155.
Szabo, J., Cowan, W.M., 1984. A stereotaxic atlas of the brain of the cynomolgus monkey (Macaca fascicularis). J. Comp. Neurol. 222, 265–300.
Van Der Gucht, E., Youakim, M., Arckens, L., Hof, P.R., Baizer, J.S., 2006. Variations in the structure of the prelunate gyrus in Old World monkeys. Anat. Rec. A Discov. Mol. Cell. Evol. Biol. 288, 753–775.
Worbe, Y., Sgambato-Faure, V., Epinat, J., Chaigneau, M., Tandé, D., François, C., Féger, J., Tremblay, L., 2013. Towards a primate model of Gilles de la Tourette syndrome: Anatomo–behavioural correlation of disorders induced by striatal dysfunction. Cortex 49, 1126–1140.